Experimental and Computational Study of the Interaction Between a Tandem-Rotor Helicopter and a Ship

Ganesh Rajagopalan
rajagopa@iastate.edu
Iowa State University
Ames, IA

Saeid Niazi
saeid@sukrahelitek.com
Sukra Helitek, Inc.
Ames, IA

Alan J. Wadcock
awadcock@mail.arc.nasa.gov
Aerospace Computing, Inc.
Moffett Field, CA

Gloria K. Yamauchi
gloria.k.yamauchi@nasa.gov
NASA Ames Research Center
Moffett Field, CA

Mark J. Silva
mark.silva@navy.mil
Naval Air Warfare Center
Patuxent River, MD

Abstract

The aerodynamic interaction between a tandem-rotor helicopter and an amphibious assault ship is investigated experimentally and computationally. The experiment was conducted in the Army 7- by 10-Ft Wind Tunnel at NASA Ames Research Center. Particle Image Velocimetry (PIV) was used to acquire 3-component velocity field measurements of the combined wake of the tandem-rotor helicopter and ship. The measured velocity fields are compared with calculations from the unsteady, incompressible flow solver Rot3DC. The Rot3DC simulation closely modeled the experimental installation, including wind tunnel walls. Comparisons are made for an equivalent full-scale wind speed of 35 knots, model yaw angle of 0 degrees, and different positions of the tandem-rotor helicopter. Comparisons between measured and calculated velocities are good, demonstrating the potential of Rot3DC in providing airwake information complementing the measured test matrix.

Introduction

In 1999 during shipboard compatibility trials, a V-22 aircraft on the deck of an L-class ship, with rotors turning, experienced an uncommanded roll in response to another rotorcraft landing upwind of the V-22. The uncommanded roll of the V-22 was classified as a deficiency requiring correction prior to operational deployment. To resolve this V-22 Roll-On-Deck (ROD) problem, the V-22 Integrated Test Team (ITT) at NAVAIR launched a comprehensive multi-phase program consisting of mathematical-model development and validation in parallel with full-scale ground-based and shipboard down-wash surveys and interaction testing. The program led to the design, implementation and demonstration of a successful fix.

One component of the multi-phase program included joint NAVAIR/Army/NASA wind tunnel investigations of the V-22 shipboard interactional aerodynamic phenomenon sponsored by the V-22 Program Office. The objectives of the V-22 ROD wind tunnel investigations were: 1) identify critical combinations of upwind aircraft position and wind-over-deck conditions based on measured roll moment response of an on-deck V-22, and 2) quantify the flowfield disturbance generated by the combined wake of the upwind rotorcraft and the ship for various rotorcraft operating upwind of an on-deck V-22 for use in an analytical study of the aircraft dynamic response. The wind tunnel tests were designed to acquire data for three primary installa-

[0]Presented at the American Helicopter Society 61st Annual Forum, Grapevine, TX, June 1-3, 2005.

tions: isolated ship, isolated aircraft, and ship plus on-deck V-22 with upwind rotorcraft. References [1, 2] describe the first wind tunnel entry (completed in April 2002) of this joint investigation. Reference [3] describes measurements of the combined wake of the ship plus upwind tandem-rotor helicopter, in addition to limited isolated ship airwake measurements. The second wind tunnel entry, concluded in November 2003, investigated the combined wake of the ship and an upwind aircraft, with the upwind aircraft being either a tilt rotor or a single main-rotor helicopter. References [4, 5] document this second test. Both wind tunnel entries were conducted in the Army 7- by 10-Foot Wind Tunnel at NASA Ames Research Center using 1/48th-scale models.

The focus of this paper is the combined wake of the ship plus upwind tandem-rotor helicopter. Using Particle Image Velocimetry (PIV), 3-component velocity measurements were acquired at several landing spots along the ship deck for various wind speeds and ship yaw angles. The wind tunnel is an ideal environment for acquiring ship airwake data since the problems of variability in wind, sea state, and atmospheric conditions that plague full-scale sea trials do not exist. However, limited test time and geometric constraints of the model installation in the tunnel are obstacles to fully exploring the desired test conditions. A validated analysis that can fill in gaps of the experimental test matrix is therefore highly desirable. Progress has been made in simulating multiple aircraft in a shipboard environment. For example, MAST and FLIGHTLAB, Refs. [6] and [7], respectively, are multi-aircraft simulation tools that have been successfully correlated with measured full-scale CH-46 downwash surveys on board an LHA. The full-scale downwash surveys consisted of discrete anemometer measurements, in contrast to a plane of velocity measurements acquired during the present small-scale study.

The present investigation uses a subset of the PIV data from the 7- by 10-Foot Wind Tunnel test to assess the ability of a low-fidelity analysis tool, Rot3DC, to predict the velocity fields at a typical V-22 landing spot on the ship deck. Rot3DC, (Ref. [8]) is an unsteady, incompressible flow solver used for rotorcraft applications. For this investigation, Rot3DC uses laminar flow and a Cartesian grid system that simplifies the problem set-up by approximating solid surfaces as stair-stepped surfaces. This grid system results in a compromised model geometry but provides a computationally economical solution. Despite the low-fidelity approach, Rot3DC has proved to be a useful and efficient tool for predicting trends of rotorcraft aeromechanic phenomena (Ref. [9]). As a precursor to the present study, Rot3DC calculations were compared with the measured isolated ship airwake velocity fields in Ref. [10]. The measured velocity fields were acquired during the isolated ship airwake testing as described in Refs. [1, 2]. The comparisons were favorable demonstrating the utility of Rot3DC, albeit for a less complicated simulation than the present study.

The remainder of this paper describes the experimental set up, the computational simulation of the experiment, and the test conditions. Comparisons between measured and computed velocity fields are presented at a typical V-22 landing spot on the ship deck.

Facility and Model Description

Facility

The tandem-rotor helicopter and ship airwake data were acquired in the 7- by 10-Foot Wind Tunnel, a closed circuit wind tunnel operated by the U. S. Army Aeroflightdynamics Directorate at NASA Ames Research Center. The test section is 7-ft high and 15-ft long. The test section width is initially 10 ft but each sidewall diverges 1/4-degree to compensate for the effects of boundary layer growth. The tunnel has a maximum speed of approximately 350 ft/s. Four high-loss turbulence-reduction screens are installed in the return duct. The test section turntable is capable of yaw angles up to 360 degrees.

Ship

The ship was designed and built at NASA Ames Research Center and is a low-fidelity 1/48th-scale model of an LHA amphibious assault ship. Reference [11] provides details of the design methodology and construction of the model ship. Figure 1 shows the ship installed in the 7- by 10-Foot Wind Tunnel. The ship was mounted on the turntable 15 inches off-axis in the wind tunnel to accommodate upwind rotorcraft simulated flight patterns flown off the port side of the ship. The turntable enabled model yaw.

The model-scale flight deck has several sets of markings known as "crow's foot" markings that duplicate full-scale markings at each landing spot (Fig. 2). These markings provide visual cues to the pilot during shipboard rotorcraft approach, hover, descent and departure sequences. Each crow's foot marking, at full scale, consists of 2 ft-wide white stripes that extend 10 to 30 ft laterally, forward,

and diagonally inwards from the landing spot center. Equivalent line width at model scale is 0.5 inches. Each crow's foot is normally associated with a set of nose-wheel and landing gear wheel spots. At model scale, the nose-wheel markings are 1-inch downstream of each crow's foot. Numerous landing spot markings are visible in Fig. 1.

Tandem-Rotor Helicopter

The basic geometry (rotor diameter, solidity, rotor-rotor position) of a CH-46 provides the primary dimensions for the tandem-rotor helicopter model. Characteristic dimensions of the approximate 1/48th-scale model are provided in Table 1. The rotor transmissions are radio-controlled model helicopter tail-rotor assemblies. The three-bladed hubs have counter-clockwise rotation on the forward rotor and clockwise rotation on the aft rotor (viewed from above). The model has rigid hubs with collective control only (no cyclic pitch control). Differential collective pitch can be introduced to trim pitching moment if so desired. Available motor power limited the tip speed of the model to 1/3 that of full-scale.

The model was mounted on a 0.75-inch six-component Task balance to measure aircraft forces and moments. Figure 3(a) shows the tandem-rotor helicopter model, plus fuselage, sting-mounted from a streamlined strut suspended beneath the tunnel traverse system. The survey apparatus is computer-controlled allowing the helicopter to be placed at any desired position alongside the ship. The streamlined strut has a fixed orientation with respect to the free-stream direction. The sting, however, can be manually rotated to deliver pre-set yaw angles of the upwind aircraft. This allows the upwind aircraft to "fly" an approach parallel to the longitudinal axis of the ship while maintaining minimum aerodynamic interference from the support hardware. The aircraft pitch attitude was fixed at zero. The aft rotor tip-path-plane was horizontal. Figure 3(b) provides details of the model CH-46 geometry.

On-Deck Tiltrotor

The geometry of the on-deck tilt-rotor model, an approximate 1/48th-scale model of a V-22 Osprey, is detailed in Ref. [11]. This on-deck aircraft was mounted on a fixed pedestal sting attached to the ship deck so as to position the tilt-rotor at either Landing Spot 7 (Fig. 4) or Landing Spot 8. During the PIV measurements at Landing Spot 7, this model remained mounted at Spot 8, but was nonoperational. Any upstream influence of the stationary (non-rotating) on-deck tilt-rotor on the PIV measurement plane is assumed to be negligible.

PIV Installation

A complete description of the PIV installation is provided in Ref. [3]. The laser light sheet (LLS) was positioned in the cross-flow plane at a fixed streamwise location in the tunnel. The ship was translated streamwise in order to document the flowfield at multiple deck locations. This eliminated the need for multiple camera calibrations. A very large measurement field was required to cover both ship airwake and the wake from the rotorcraft flying approach patterns off the port side of the deck during other phases of the experiment. The PIV flow field was therefore centered in the test section despite the ship being mounted off-axis. The PIV flow field size was approximately 6-ft wide by 3-ft high.

A Spectra Physics PIV 400 dual-oscillator Nd:Yag laser with 350 mJ/pulse at 532 nm wavelength was used for the PIV measurements. Two high-resolution Kodak ES 4.0 2k x 2k digital cameras were used in order to provide the desired spatial resolution. These cameras were used in forward scatter, 30 degrees off-axis, in order to provide optimal particle visibility whilst maintaining acceptable perspective in the image. Each camera was equipped with a 50 mm f/1.4 Nikkor lens mounted on motorized rotation and translation stages to satisfy the Scheimpflug focusing condition.

A single Corona Integrated Technologies Vicount 5000 2.2 kW Series 180 mineral oil smoke generator was used to seed the flow. The nominal LLS thickness was 6 mm. The maximum out-of-plane particle displacement was kept small (less than 25% of the LLS thickness) in order to provide a strong correlation. In-plane particle displacements were kept below 4 pixels. Once satisfactory conditions were met, 100 frames of data were acquired for each test condition. The data were processed with a 24-pixel cross-correlation window. The corresponding spatial resolution of the measurements is 0.8-in horizontal and 0.4-in vertical (equivalent full-scale spatial resolutions of 3.4 ft and 1.7 ft, respectively).

Analysis Description

The analysis used here is Rot3DC (Rotor 3-D Code), developed by Sukra Helitek, Inc. to simulate rotorcraft flow fields. This package applies special techniques to generate the flow through the rotor in different flight regimes. Flow characteristics, including rotor wake flows and rotor

performance, computed with this method correlate well with available experimental and analytical databases [8, 12, 13, 14, 15, 16, 17, 18, 19]. The technique is versatile, computationally economical and particularly suitable for configurations with multiple rotors and for rotor-body interacting flows. Rot3DC has been used as an analysis tool for complex configurations such as Bell Helicopter's Quad Tiltrotor [20], Boeing's Dragonfly X-50 [21] and to gain insight into complex aerodynamic phenomena such as tilt rotor aircraft pitch-up with side slip [9].

Flow Algorithm

For all calculations presented in this paper, the flow field was assumed to be incompressible and laminar. The rotor was modeled as a momentum source [14, 15, 16] in this analysis. To explain the overall rotor source evaluation procedure, the unsteady, Cartesian, incompressible, laminar equations are quoted below.

mass:

$$\frac{\partial u}{\partial x} + \frac{\partial v}{\partial y} + \frac{\partial w}{\partial z} = 0 \tag{1}$$

x momentum :

$$\rho \frac{\partial}{\partial t}(u) + \rho \left(u\frac{\partial u}{\partial x} + v\frac{\partial u}{\partial y} + w\frac{\partial u}{\partial z} \right) = \mu \left(\frac{\partial^2 u}{\partial x^2} + \frac{\partial^2 u}{\partial y^2} + \frac{\partial^2 u}{\partial z^2} \right) - \frac{\partial p}{\partial x} + S'_x \tag{2}$$

y momentum :

$$\rho \frac{\partial}{\partial t}(v) + \rho \left(u\frac{\partial v}{\partial x} + v\frac{\partial v}{\partial y} + w\frac{\partial v}{\partial z} \right) = \mu \left(\frac{\partial^2 v}{\partial x^2} + \frac{\partial^2 v}{\partial y^2} + \frac{\partial^2 v}{\partial z^2} \right) - \frac{\partial p}{\partial y} + S'_y \tag{3}$$

z momentum :

$$\rho \frac{\partial}{\partial t}(w) + \rho \left(u\frac{\partial w}{\partial x} + v\frac{\partial w}{\partial y} + w\frac{\partial w}{\partial z} \right) = \mu \left(\frac{\partial^2 w}{\partial x^2} + \frac{\partial^2 w}{\partial y^2} + \frac{\partial^2 w}{\partial z^2} \right) - \frac{\partial p}{\partial z} + S'_z \tag{4}$$

where S'_x, S'_y, and S'_z are the time averaged rotor source terms per unit volume due to the rotor motion in the coordinate directions x, y, and z, respectively. S'_x, S'_y, and S'_z are added to other source terms that may exist in the flow field. The source terms are time-averaged for convenience but this is not a requirement of the method itself. These source terms denote the rotor-induced force per unit volume at a point and it is through these terms that the rotor influence is introduced into the flow field. At the beginning of the computation the sources are assumed to be zero and they evolve as the iterations proceed.

The numerical algorithm for solving the governing equations of the flow is based on Patankar's "SIMPLER" algorithm [22]. In this procedure, the primitive variables, the static pressure and the components of velocity, are obtained directly by solving the mass and momentum conservation equations (the Navier-Stokes equations).

Rotor Sources

As mentioned earlier, the action of the rotor blades is modeled in this formulation through the momentum equation sources (S'_x, S'_y and S'_z) in the coordinate directions. The strength of the rotor source at a specific location through which the blade is passing is a function of the local flow conditions, the physical location, and the geometric and aerodynamic characteristics of the rotor blades. In functional notation, the time-dependent discretized source terms can be written as follows:

$$S_i = S_i(C_l, C_d, \alpha, \vec{V}_{abs}, \omega, x, y, z, t, c, \rho, \mu, Re, M, N) \tag{5}$$

where i=1, 2, 3 and i denotes the x, y and z directions; C_l and C_d are airfoil characteristics of the rotor blade; and N is the number of blades.

These source terms are not known a *priori* and are a highly desired result of any rotor solution procedure. The details of the development of these source terms are available in Refs. [14, 15, 16].

Time Averaging and Coupling

Next, we consider the time averaging procedure used to simplify the analysis. As the blades rotate, they develop a force distribution along the blades. If $\vec{F}$ is the resultant aerodynamic force vector on the blade at a given section, $-\vec{F}$ is the instantaneous force vector acting on a fluid element at any location (x,y,z), which must be added to the momentum equation as an external force acting on the fluid. However, for a time averaged solution, only a fraction of this force is to be added at a computational cell. This fraction is determined as follows. The time taken by the center of the blade element at a rotational speed of ω to traverse one revolution is:

$$t_{1.rev} = \frac{2\pi}{\omega} \tag{6}$$

The time the center of a blade element spends in a given control volume of width $\Delta\theta$ radians is:

$$t_{\Delta\theta} = \frac{\Delta\theta}{\omega} \tag{7}$$

Therefore, the fractional time that the blade element spends in a cell is:

$$t_{frac} = \frac{\Delta\theta}{2\pi} \quad (8)$$

For a rotor with N blades the time averaged source term to be added to the momentum equation is

$$\vec{S} = (S_x, S_y, S_z) = \frac{N\ \Delta\theta}{2\pi}\left(-\vec{F}\right) \quad (9)$$

The source terms are grid specific and are calculated from the velocity field of the previous iteration level. Figure 5 summarizes the coupling of the SIMPLER algorithm and the rotor source term calculations.

Computational Simulation of Experiment

The layout of the computational grid, boundary conditions, process for computing aircraft thrust and computational requirements are described in the following sections.

Grid

Rot3DC employed a single-block, 3D Cartesian grid system. This grid system prevents the grid from fitting precisely around curved surfaces. The (X, Y, Z) coordinate system was fixed with respect to the wind tunnel. The origin of the coordinate system is shown in Fig. 6. The X-direction (positive in the freestream direction) is parallel to the wind tunnel walls. Z is measured positive upwards from the water line (i.e., the wind tunnel floor). The single-block grid (Fig. 6) was divided into four sections: ship grid, CH-46 grid, PIV grid, and the surrounding boundary grid. The boundary grid was modeled as a rectangular duct of constant cross-section. The boundary grid extends 12 ship-widths in front of and behind the ship. The ship grid zone occupies a volume that contains the ship. Similarly, the CH-46 grid zone contains the CH-46, and the PIV grid zone contains the plane matching the location of the PIV data. For the ship grid zone, the X-grid has nonuniform grid spacing while a uniform grid spacing in Y and Z was used. For the ship grid zone, spacings of 0.38 in$<\Delta$X$<$ 1.67 in, ΔY = 0.72 in, and ΔZ = 0.228 in were used. Within the CH-46 and PIV grid zones, uniform spacing was used. For the CH-46 grid zone, ΔX = 0.38 in, ΔY = 0.38 in, and ΔZ = 0.228 inch. Within the PIV zone, ΔX = 0.97 in, ΔY = 0.72 in, and ΔZ = 0.228 in were used. Nonuniform grid spacing was used to smoothly transition between zones, with finer grid spacing (in X, Y, and Z) adjacent to zone edges. The maximum cell width ratio between two adjacent cells in the ship and CH-46 grid zones was approximately 1.3. For the three cases simulated for this paper, typical overall grid dimensions were 169x173x115 (3.4 million grid points).

The CH-46 fuselage used in the experiment was a flexible piece of plastic wrapped around the frame of the model (Fig. 3(a)). The CH-46 geometry used for the simulation was obtained by scaling the full-scale CH-46 dimensions by 1/48. The ship geometry was based on the 1/48th-scale ship dimensions. Initially, the wind tunnel traverse support members and the CH-46 sting were modeled, as shown in Fig. 7(a). Later, because non-body fitted grids were used for computational efficiency and the number of grid points allotted to the traverse support members was severely limited by computational resources, the decision was made to run the simulations with just the ship, CH-46, and wind tunnel walls (see Fig. 7(b)).

As shown in Fig. 1, the ship is large compared to the wind tunnel test section. Reference [10] examined the blockage of the isolated ship by comparing velocity fields at different longitudinal stations above the ship, with and without wind tunnel walls. For a ship yaw angle of 0 deg, wall effects account for an approximate 7.3% increase in the streamwise velocity component above the deck at Landing Spot 7. The presence of the wind tunnel walls, however, was found to have minimal effect on the vertical velocity at the V-22 rotor tip-path plane height at Landing Spot 7 or 8.

Boundary Conditions

The parallel simulated wind tunnel side walls were treated as inviscid surfaces since the actual wind tunnel walls incorporate a small divergence to account for boundary layer growth. The wind tunnel ceiling and ground plane do not diverge and so viscous no-slip conditions were imposed at these surfaces. At the inlet, free-stream conditions were imposed. All solid bodies were treated as blocked cells with no flow through them and viscous, no-slip conditions applied at the body surface. The outlet boundary, a plane parallel to the inlet boundary, is left for the numerical scheme to compute with mass conservation strictly enforced.

Aircraft Thrust Computation

As mentioned earlier, Rot3DC calculates rotor thrust using the computed velocity field and tabulated airfoil data for the lift and drag coefficients. A low Reynolds number airfoil was designed specifically for the model CH-46 rotor blade (Ref. [2]). Airfoil lift and drag coefficients were calculated us-

ing 2-D analyses. NACA 0012 airfoil characteristics were used to fill in gaps in the C81 table for the low Reynolds number airfoil.

The following procedure was used to establish the aircraft thrust coefficient in the simulation. A collective sweep was performed for the isolated CH-46 (without fuselage) in hover. The relationship between rotor thrust coefficient and collective pitch was defined from this sweep. Next, a CH-46 rotor collective was chosen based on the collective sweep computed for hover and the target aircraft thrust coefficient. The simulation of the CH-46 and ship in the wind tunnel was then performed at the desired advance ratio. The vertical force on the fuselage was calculated and subtracted from the thrust generated by the two CH-46 rotors, resulting in the aircraft thrust. This procedure required 1-2 iterations to achieve the desired aircraft thrust coefficient at the desired advance ratio.

Computational Requirements

The time step for one iteration was chosen as 0.01 second. Based on previous experience on modeling isolated ship airwake, each iteration had 10 sub-iterations. Each simulation was run for 13 s of real time. One second of real time required approximately 20 hours of CPU time and 1 GB of storage. Unless otherwise specified, solutions presented in this paper are time averaged over the last 3 seconds of the simulation. For a freestream velocity of 19.7 ft/s, 3 seconds of computation allows a released particle to travel more than 3 times the ship length. The total time of the simulation allows for at least one complete air exchange within the computational domain. The simulations were run on PCs using a Linux OS with 2.0 GB of memory and a 3.4 GHz Intel Pentium V processor.

Test Conditions

The motivation behind the PIV measurements was to understand the aerodynamic interactions influencing an on-deck V-22 due to either the isolated ship airwake or the combined wake of the ship and an additional aircraft operating upwind. Reference [3] explored these interactions in detail. For the present study, three test conditions for yaw = 0 deg presented in Ref. [3] are chosen for comparison with Rot3DC calculations. For all three cases, the CH-46 is located longitudinally at Landing Spot 6 and the resulting velocity field in a vertical cross-flow plane at Landing Spot 7 is examined. The plane is coincident with a plane intersecting the hub centers of a virtual on-deck V-22 (Fig. 8). Variations in CH-46 lateral and vertical position are explored.

Using the wind tunnel traverse system, the tandem-rotor helicopter was positioned using the geometry shown in Fig. 9. The lateral position of the CH-46 is presented in terms of b/2, where b is the V-22 wing span. In Fig. 9, y = 0 corresponds to the CH-46 positioned directly in front of the virtual V-22 and y = b/2 corresponds to the CH-46 positioned in front of the virtual V-22 left rotor. Vertical position of the CH-46 is identified using the CH-46 wheel height over deck (WHOD). When the CH-46 nose wheel is on the deck (WHOD = 0), the aft rotor tip-path-plane of the CH-46 is 5.06 in (20.24 ft full-scale) above the deck.

The helicopter was trimmed to an aircraft CT of approximately 0.0048 (full-scale gross weight of 20,800 lb) before the PIV data were acquired. The rotor speed, as mentioned previously, was one-third full-scale tip speed. Desire to match the full-scale advance ratio dictated the freestream speed. All comparisons are made for a freestream velocity of Uinf = 19.7 ft/s (35 knots equivalent full-scale).

Results

Velocity fields, representing the averaged flow field over the last 3 sec of the computational simulation, are presented in the cross-flow plane. The streamwise (out of plane) velocity component, normalized with the free stream velocity Uinf, is presented in the form of iso-velocity contours. In-plane velocity components, scaled with the free stream velocity, are presented as velocity vectors. For the computed velocity plots, 25% of the in-plane velocity vectors are shown for clarity. For the PIV plots 11% of the velocity vectors are shown. Since the flowfield near the V-22 rotors is of particular interest for the V-22 ROD problem, the tip-path-plane of the V-22 rotors, the outline of the ship deck, the outline of the CH-46 rotors, and the outline of the superstructure are included as appropriate in figures to assist in interpreting the flowfield. The CH-46 is located longitudinally at Landing Spot 6 for all three cases examined. All dimensions are presented in full-scale equivalent coordinates.

CH-46: WHOD = 10 ft, y = 2(b/2)

Figure 10 shows the evolution of the aircraft thrust coefficient for the 13 s simulation of the CH-46 operating at a WHOD of 10 ft and nose wheel location of y = 2(b/2). For comparison, the thrust from each rotor as well as the combined thrust from both rotors is also shown. The download generated

by the rotors can be determined by subtracting the aircraft thrust from the combined thrust of both rotors. The download is approximately 10% of the total rotor thrust. After 2 seconds, the calculated aircraft thrust coefficient has reached a steady value of approximately 0.0049 which is about 2% higher than the experimental value of 0.0048.

Figure 11 presents the time-averaged calculated flow field at Landing Spots 7 and 8 (the usual landing locations for the V-22). The cross-flow planes in Fig. 11 intersect the hubs of a virtual on-deck V-22 positioned at either Landing Spot 7 or 8. The wake of both the ship superstructure and the CH-46 are noticeably weaker at Landing Spot 8 compared with Landing Spot 7.

Figures 12(a) and 12(b) show the calculated and measured velocities, respectively, in a cross-flow plane intersecting the hubs of a virtual on-deck V-22 at Landing Spot 7. In addition to the outline of the ship deck and superstructure, the fore and aft rotor disks of the tandem-rotor helicopter are also shown. The downwash imposed on an on-deck tilt-rotor at Spot 7 can be determined by identifying the position of the left and right V-22 rotors in black. A wheel height of 10 ft for the CH-46 corresponds to the aft rotor tip-path-plane being at a full-scale height of 30.24 feet. Both the calculated and measured flow fields show a single counter-rotating vortex pair generated by the CH-46. Each rotor disk of the tandem-rotor helicopter is assumed to generate a wake that resembles, in many respects, the wake from a fixed wing. Unlike the tightly rolled up tip vortices that form downstream from a fixed-wing aircraft, each rotor disk is assumed to generate a pair of "super vortices". These vortices are much larger in physical size and are assumed to take longer for complete roll-up to occur than for a fixed wing aircraft. Due to the proximity of the two rotor disks, the tandem-rotor helicopter generates only a single pair of super vortices. For both the calculated and measured results, the starboard super vortex is weaker than the port super vortex. The starboard super vortex is located above the port edge of the deck and viscous forces (the deck boundary layer) will dissipate the rotational energy of this vortex.

The calculated wake, Fig. 12(a), appears slightly higher than the measured wake shown in Fig. 12(b). Figure 12(b) shows the measured wake is located symmetrically downstream from the generating aircraft. The widths of the calculated and measured wake are both greater than the CH-46 diameter. The measured wake has expanded more than the calculated wake. The effect of the vertical strut supporting the CH-46 appears as a defect in the measured velocity field. Recall that the simulation does not include any of the traverse support members. The location of the vertical support obstructed the view of one of the PIV cameras. Hence, data downstream of the superstructure could not be acquired.

Figure 13 shows the calculated and measured vertical velocity at the virtual V-22 tip-path-plane height for Landing Spots 7 and 8. Velocities extracted at 2.5 s and 5.0 s into the simulation are also presented for Landing Spot 7. Although there are noticeable differences between the instantaneous and the averaged velocity profiles in the wake of the ship superstructure, there are only minor differences in the wake of the CH-46. The helicopter wake, for this condition, approaches a steady condition 2.5 sec into the simulation. At Landing Spot 7, the starboard vortex of the CH-46 wake imposes a downwash at the V-22 left rotor, creating a left-wing down rolling moment of the V-22. By comparing the peak-to-peak velocity difference of the starboard vortex to that of the port vortex, we see that the difference in strength between the two vortices is more pronounced for the calculated flow field compared to the measurements. In addition, the port vortex in the measured flow field is farther to the left than in the simulation but the calculated strength is in good agreement with measurements. The calculated position of the starboard vortex matches the measured location, although the strength is underpredicted. In summary, however, the calculated vertical velocity matches the measurements reasonably well. At Landing Spot 8, the strength of the calculated supervortices is about half compared to their strength at Landing Spot 7. Figure 11 and Fig. 13 show that the starboard vortex is further to the right at Landing Spot 8 compared with Landing Spot 7. The vortex movement could be caused by either entrainment into the superstructure wake or the image vortex in the deck (once the vortex moves above the deck).

CH-46: WHOD = 10 ft, y = 4(b/2)

Figure 14 is similar to Fig. 11 except that the CH-46 is now positioned further to port at y = 4(b/2). The wake of the CH-46 is now completely clear of the ship. Figures 15(a) and 15(b) show the calculated and measured velocity fields. Figure 15 shows strong entrainment into the superstructure wake. The wake from the helicopter is shown off the port side of the deck. The calculated flowfield shown in Fig. 15(a) shows very little downwash from the rotor wake above the deck. Experimental measure-

ments above the ship deck were not obtained due to one of the PIV cameras having an obstructed view (Fig. 15(b)).

Figure 16 shows the calculated and measured vertical velocity at the virtual V-22 tip-path-plane height. Like Fig. 13, Fig. 16 shows that the CH-46 wake at Landing Spot 7 is steady after 2.5 s of the simulation. By moving the CH-46 to the y=4(b/2) location, the starboard vortex now creates a weak upwash at the V-22 left rotor. The CH-46 rotor wake has become more symmetric because the starboard super vortex is no longer affected by the deck boundary layer. Note that the starboard and port vortices in Fig. 16 are closer in strength compared to the case of Fig. 13. This holds true for both the calculated and measured flowfields. The calculated and measured positions of the starboard vortex are in good agreement. The measured port vortex, however, remains further to the left of the calculated vortex (similar to Fig. 13). At Landing Spot 8, the calculation shows that the strength of the vortices is reduced compared to Landing Spot 7 and the wake has expanded slightly.

CH-46: WHOD = 40 ft, y = 2(b/2)

Figure 17 is similar to Fig. 11 except that the CH-46 height above deck has been increased by 30 ft full-scale. Figure 18 compares the calculated and measured flowfields. The calculated wake shown in Fig. 18(a) is noticeably higher and narrower than the measured wake in Fig. 18(b). The calculated lateral location of the starboard vortex, however, is in fair agreement with the measurements. The measured wake shows the starboard supervortex just above the left V-22 rotor causing a strong downwash through the left rotor; calculations show a much smaller downwash. Comparing Figs. 12 and 18, we find that an increase in the CH-46 WHOD of 30 ft causes an increase in height of approximately 32 ft and 25 ft, respectively, for the calculated and measured wake.

Figure 19 shows vertical velocity profiles at the tip-path-plane height of the virtual V-22. The instantaneous velocity profiles at Landing Spot 7 are indistinguishable from the average velocity profile in the CH-46 wake. The calculated wake at Landing Spot 7 is offset both vertically and laterally compared to the measured wake, hence the calculated and measured vertical velocity profile do not agree.

Figure 20 shows velocity profiles at several heights above the deck including the V-22 tip-path plane height of 20.8 ft shown in Fig. 19. Figure 20 shows that at a height of 50.8 ft above the deck, the calculated vertical velocity profile is similar to the measured profile acquired at 20.8 feet above the deck. The reason for the discrepancy between the calculated and measured wake heights is unclear. Rot3DC has been used in the past to successfully predict wake trajectories of full-scale helicopters. Therefore, there may be an effect of scale on the calculated wake skew angle or the problem may reside in the experimental data. An investigation of wake skew angle as a function of aircraft height above deck may help shed light on the problem. Currently, there is insufficient information to identify the reason for the disagreement.

Conclusions

The aerodynamic interaction between a tandem-rotor helicopter and an amphibious assault ship was investigated experimentally and computationally. Flow field comparisons are made for an equivalent full-scale wind speed of 35 knots, model yaw angle of 0 degrees, and three different positions of the tandem-rotor helicopter. Comparisons between measured and calculated velocities at the tip-path-plane height of a virtual on-deck V-22 are good when the helicopter wheel-height above deck is 10 feet. The location and strength of the super-vortex pair generated by the helicopter is predicted well enough to provide airwake information complementing the measured test matrix for this wheel height. For a helicopter wheel height of 40 ft, however, the calculated wake does not descend as rapidly as the measured wake.

Acknowledgment

The authors would like to thank David Schaller of Sukra Helitek, Inc. without whose help and valuable suggestions this paper could not have been completed. The authors would also like to express their gratitude to Angela Lestari of Sukra.

References

[1] Silva, M. J., Yamauchi, G. K., Wadcock, A. J., and Long, K. R., "Wind Tunnel Investigation of the Aerodynamic Interactions Between Helicopters and Tiltrotors in a Shipboard Environment," American Helicopter Society 4th Decennial Specialists' Conference on Aeromechanics, San Francisco, CA, January 2004.

[2] Yamauchi, G. K., Wadcock, A. J., Derby, M. D., Long, K. R., and Silva, M. J., "Results

from the V-22/Ship/Helicopter Aerodynamic Interaction Phenomena (VSHAIP) Wind Tunnel Test -Part 1," NASA TM to be published, 2005.

[3] Wadcock, A. J., Yamauchi, G. K., Heineck, J. T., Silva, M. J., and Long, K. R., "PIV Measurements of the Wake of a Tandem-Rotor Helicopter in Proximity to a Ship," American Helicopter Society 4th Decennial Specialists' Conference on Aeromechanics, San Francisco, CA, January 2004.

[4] Silva, M. J., Wadcock, A. J., Yamauchi, G. K., Van Aken, J. M., and Shinoda, P. M., "Wind Tunnel Investigation of the Shipboard Aerodynamic Interactions Inducing the V-22 Tiltrotor Uncommanded Roll On-deck Response," American Helicopter Society 61st Annual Forum, Grapevine, TX, June 2005.

[5] Van Aken, J. M., Wadcock, A. J., Yamauchi, G. K., and Silva, M. J., "Results from the V-22/Ship/Helicopter Aerodynamic Interaction Phenomena (VSHAIP) Wind Tunnel Test - Part 2," NASA TM to be published, 2005.

[6] McKillip, Jr., R. M., Wachspress, D. A., Keller, J. D., Whitehouse, G. R., Quackenbush, T. R., and Boschitsch, A. H., "Distributed Multi-Vehicle Simulation Including High-Order Airwake Representation," American Helicopter Society 60th Annual Forum, Baltimore, MD, June 2004.

[7] He, C., Hong, X., and Bhagwat, M., "Advanced Rotor Wake Interference Modeling for Multiple Aircraft Shipboard Landing Simulation," American Helicopter Society 60th Annual Forum, Baltimore, MD, June 2004.

[8] Rajagopalan, R. G., "A Procedure for Rotor Flowfield and Interference: A Perspective," *AIAA 2000-0116*, 38th AIAA Aerospace Sciences Meeting, Reno, NV, January 2000.

[9] Potsdam, M. A., Schaller, D., Rajagopalan, G., and Silva, M. J., " Tilt Rotor Aeromechanics Phenomena in Low Speed Flight," American Helicopter Society 4th Decennial Specialists' Conference on Aeromechanics, San Francisco, CA, January 2004.

[10] Rajagopalan, R. G., Schaller, D., Wadcock, A. J., Yamauchi, G. K., Heineck, J. T., and Silva, M. J., "Experimental and Computational Simulation of a Model Ship in a Wind Tunnel," *AIAA 2005-1347*, 43rd AIAA Aerospace Sciences Meeting, Reno, NV, January 2005.

[11] Derby, M. R. and Yamauchi, G. K., "Design of 1/48th-Scale Models for Ship-Rotorcraft Interaction Studies," *AIAA 2003-3952*, 21st AIAA Applied Aerodynamics Conference, Orlando, FL, June 2003.

[12] Rajagopalan, R. G. and Fanucci, J. B. "Finite Difference Model for Vertical Axis Wind Rotors," *Journal of Propulsion and Power*, Vol. 1, No. 6, pp. 432-436, 1985.

[13] Rajagopalan, R. G. and Zhang, Z., "Performance and Flow Field of a Ducted Propeller," AIAA/ASME/SAE/ASEE 25th Joint Propulsion Conference, Monterey, CA, July 1989.

[14] Rajagopalan, R. G. and Lim, C. K., "Laminar Flow Analysis of a Rotor in Hover," *Journal of the American Helicopter Society*, Vol. 36, No. 1, pp. 12-23, January 1991.

[15] Rajagopalan, R. G. and Mathur, S. R., "Three Dimensional Analysis of a Rotor in Forward Flight," *Journal of the American Helicopter Society*, Vol. 38, No. 3, pp. 14-25, July 1993.

[16] Zori, L. and Rajagopalan, R. G., "Navier-Stokes Calculations of Rotor-airframe Interaction in Forward Flight," *Journal of the American Helicopter Society*, Vol. 40, No. 2, pp. 56-67, April 1995.

[17] Rajagopalan, R. G., Berg, D. E., and Klimas, P. C., "Development of a Three-Dimensional Model for the Darrieus Rotor and Its Wake," *Journal of Propulsion and Power*, Vol. 11, No. 2, pp. 185-195, March-April 1995.

[18] Rajagopalan, R. G. and Keys, C., "Detailed Aerodynamics Design of the RAH-66 Fantail Using CFD," *Journal of the American Helicopter Society*, Vol. 42, No.4, October 1997.

[19] Poling, D. R., Rosenstein, H., and Rajagopalan, G., "Use of a Navier-Stokes Code in Understanding Tiltrotor Flowfields in Hover," *Journal of the American Helicopter Society*, Vol. 42, No. 2, pp. 103-109, April 1998.

[20] Lestari, A., Niazi, S., and Rajagopalan, G., "Preliminary Analysis of a Quad Tiltrotor Flowfield and Performance," AHS Tiltrotor/Runway Independent Aircraft Technology and Applications Specialists Meeting, Arlington, TX, March 2001.

[21] Niazi, S., Rajagopalan, G., Thompson, T., and JanakiRam, R., " Simulation of Unsteady Aerodynamics of the Unmanned CRW Dragonfly Aircraft Hovering Near the Ground," AHS International Specialists' Meeting, Unmanned Rotorcraft, Design, Control and Testing, Chandler, AZ, January 2005.

[22] Patankar, S. V., "Numerical Heat Transfer and Fluid Flow," Hemisphere Publishing Corporation, 1980.

Table 1: Full-Scale and Model-Scale Tandem-Rotor Helicopter Properties.

	Full-Scale	**Model-Scale**
No. of rotors	2	2
No. blades per rotor	3	3
Rotor radius (in)	306.0	6.311
Blade tip chord (in)	18.75	0.375
Rotor solidity	0.0585	0.057
Rotor RPM (100 %)	264	4224
Tip speed (ft/s)	705	233
Blade tip Reynolds number	7.03×10^6	46,370

Figure 1: 1/48th-scale amphibious assault ship installed in the Army 7- by 10-Foot Wind Tunnel at NASA Ames.

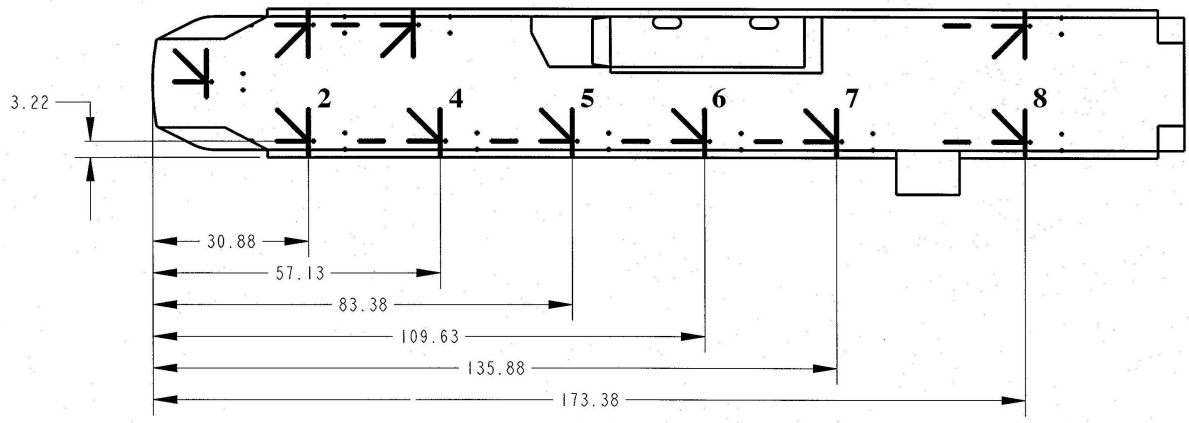

Figure 2: Landing spot locations on the 1/48th-scale amphibious assault ship (measurements shown in inches).

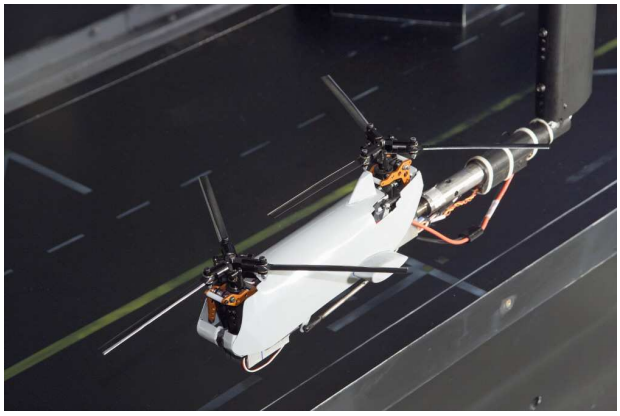

(a) Wind tunnel installation.

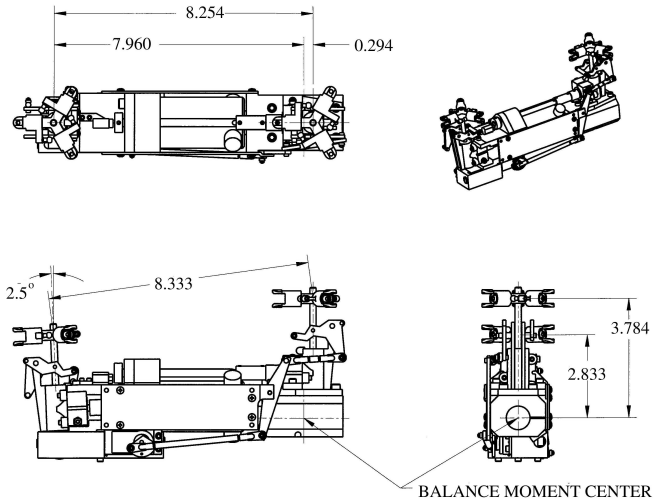

(b) Model geometry (measurements shown in inches).

Figure 3: Tandem-rotor helicopter model.

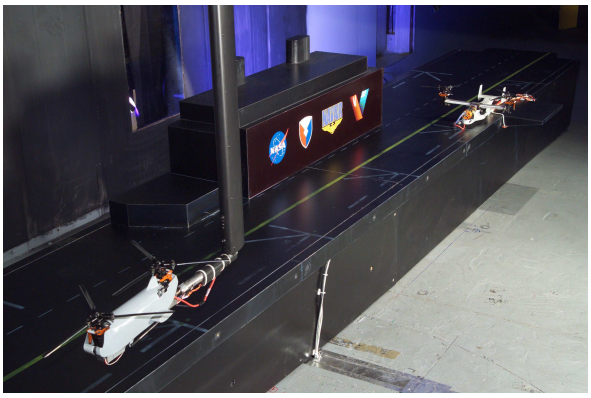

Figure 4: Tandem-rotor helicopter and on-deck tilt-rotor (at Spot 7).

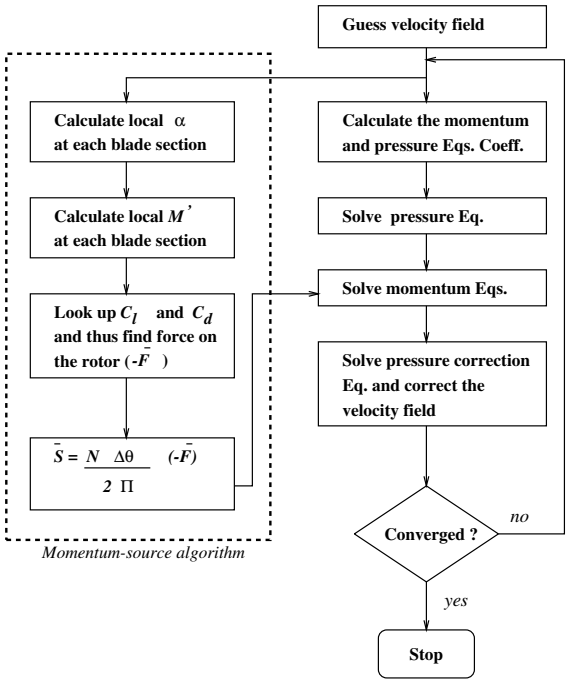

Figure 5: Coupling of SIMPLER and rotor source term calculations.

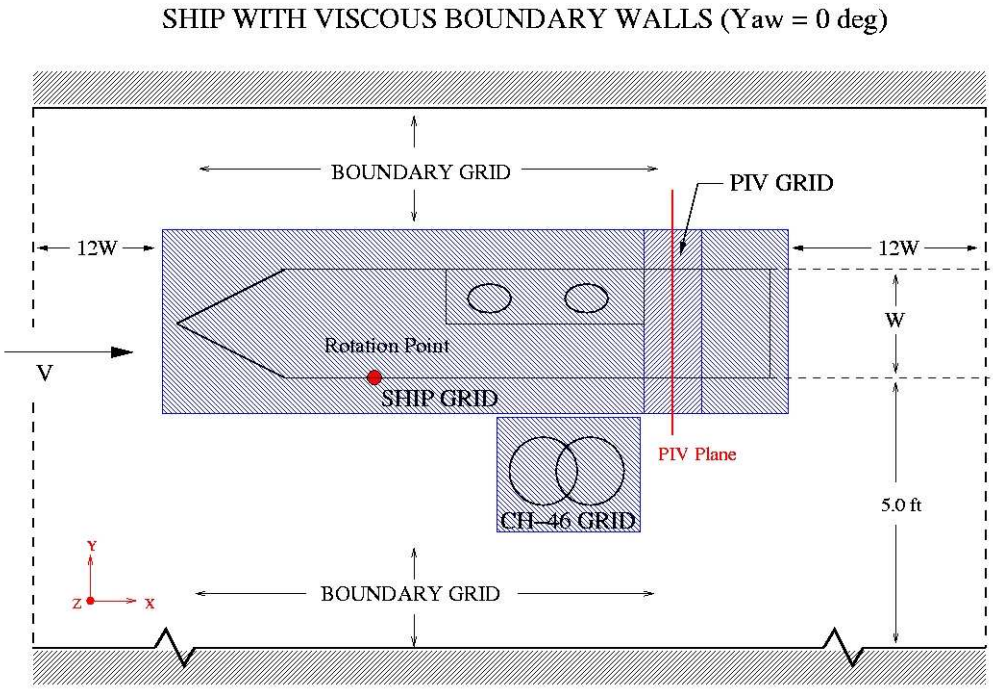

Figure 6: Schematic of grid boundaries for computational simulation.

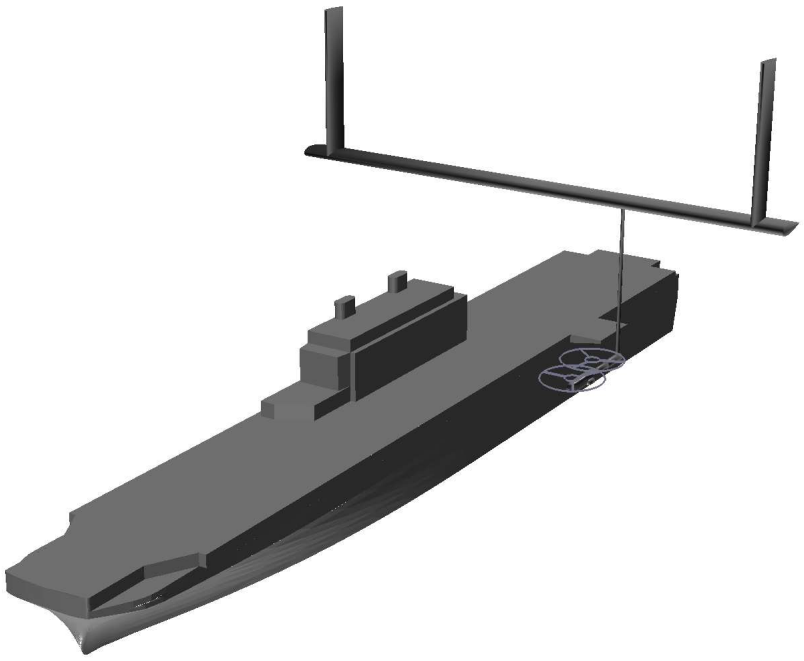

(a) Initial simulation.

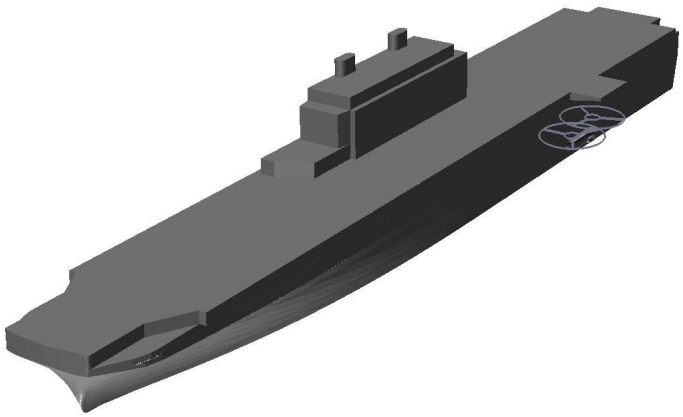

(b) Final simulation.

Figure 7: Experimental set-up as modeled in the computational simulation (wind tunnel walls modeled but not shown).

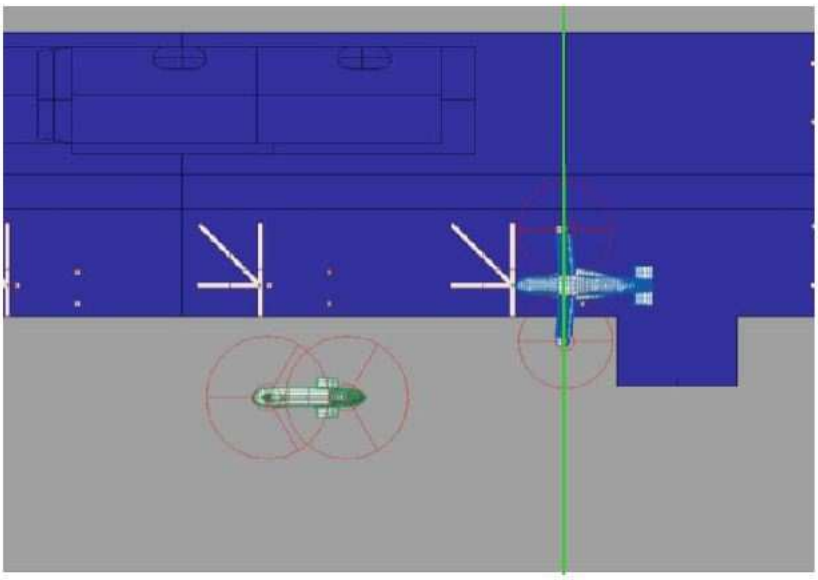

Figure 8: LLS location in wind tunnel. Virtual on deck V-22 at Spot 7. Ship and tandem-rotor helicopter model yaw = 0 deg.

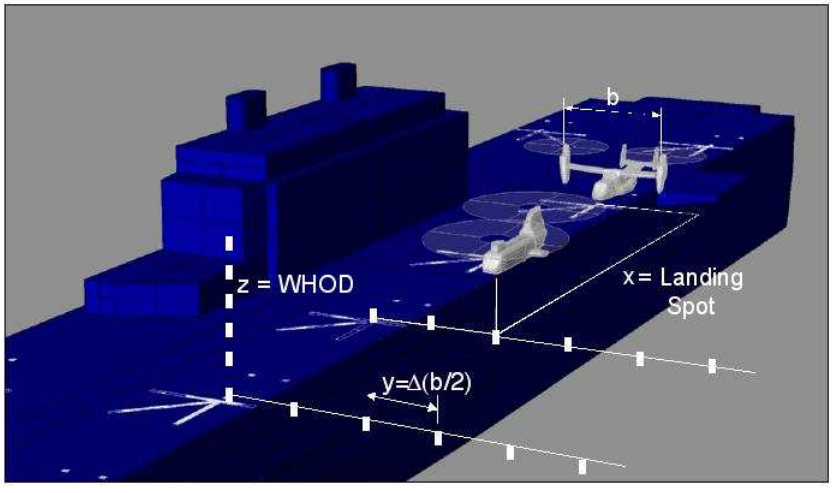

Figure 9: Geometry for mapping position of rotorcraft near or on the ship.

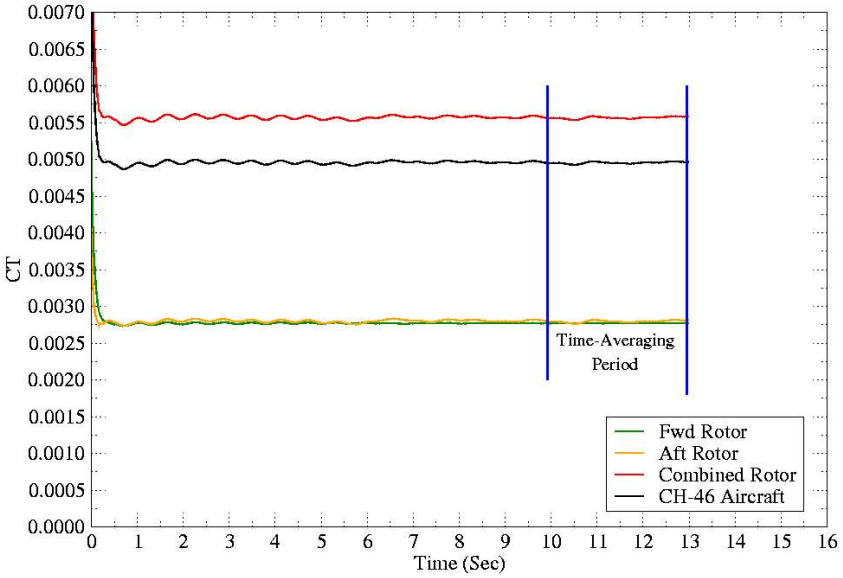

Figure 10: Time history of CH-46 thrust coefficient for yaw = 0 deg, Uinf = 19.7 ft/s (35 kts full-scale equivalent). CH-46 longitudinal location = Landing Spot 6, lateral offset = 2(b/2), WHOD = 10 ft.

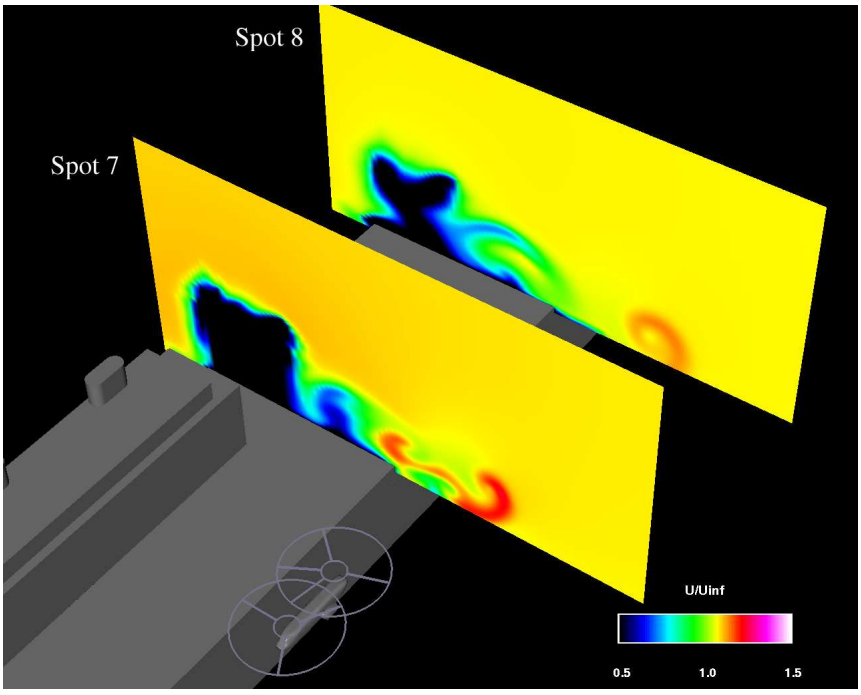

Figure 11: Calculated streamwise velocity component for yaw = 0 deg, Uinf = 19.7 ft/s (35 kts full scale equivalent). CH-46 longitudinal location = Landing Spot 6, lateral offset = 2(b/2), WHOD = 10 ft. Calculations shown for Landing Spots 7 and 8.

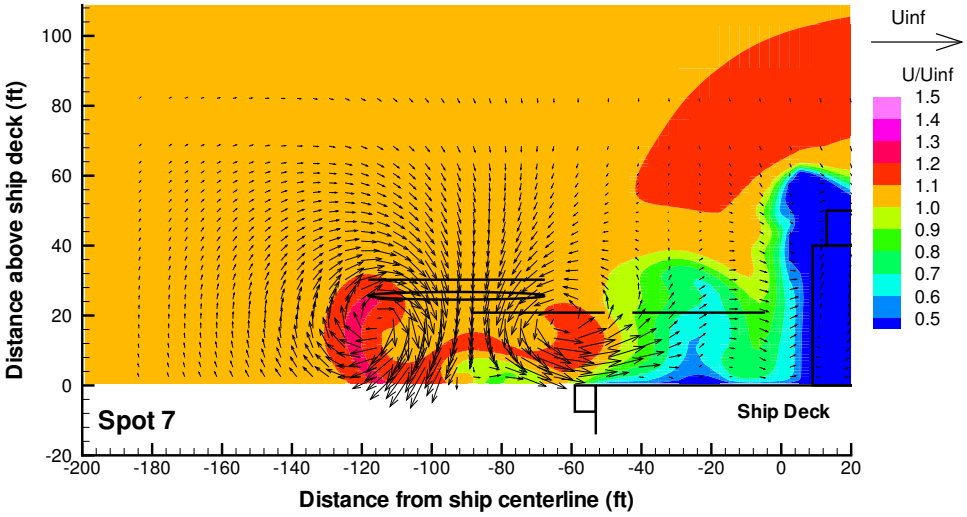

(a) Calculated.

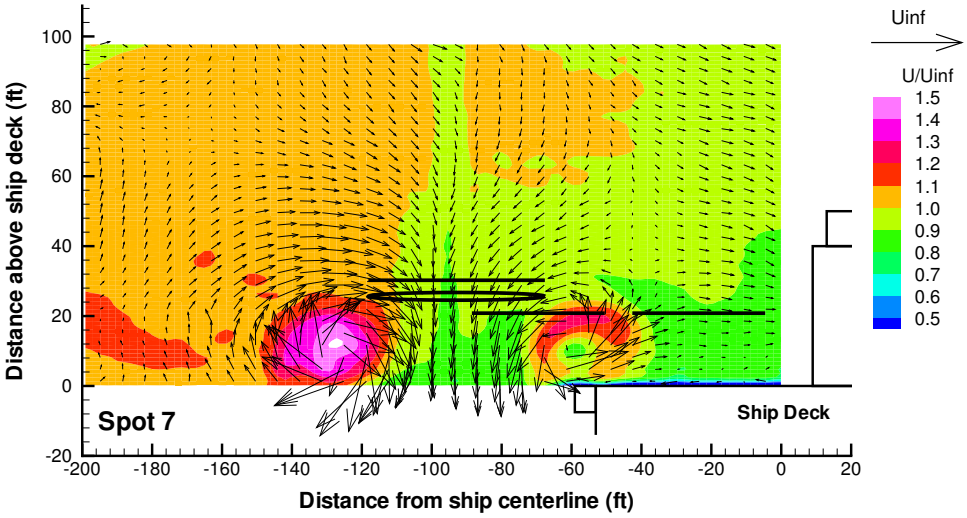

(b) PIV measurements.

Figure 12: Comparison between calculated and measured velocity fields at Landing Spot 7 for yaw = 0 deg, Uinf = 19.7 ft/s (35 kts full scale equivalent). CH-46 longitudinal location = Landing Spot 6, lateral offset = 2(b/2), WHOD = 10 ft. View looking upstream.

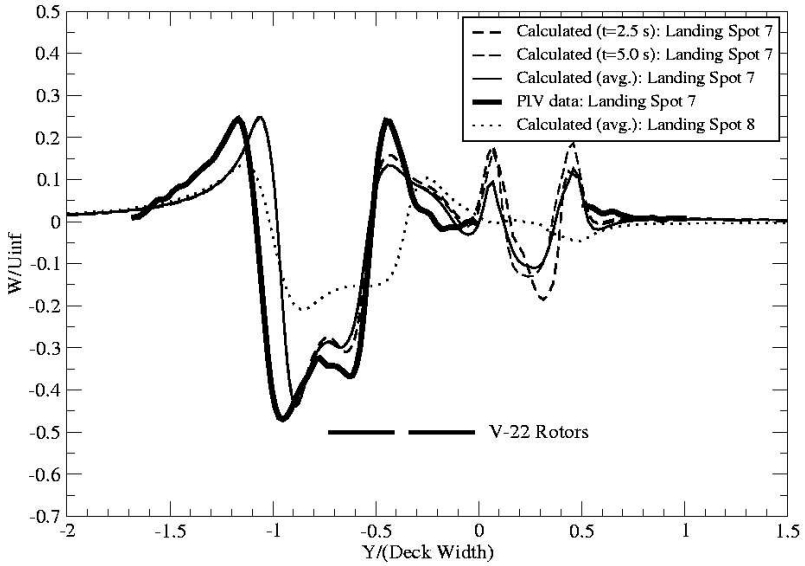

Figure 13: Comparison between calculated and measured vertical velocity for yaw = 0 deg, Uinf = 19.7 ft/s (35 kts full-scale equivalent). CH-46 longitudinal location = Landing Spot 6, lateral offset = 2(b/2), WHOD = 10 ft.

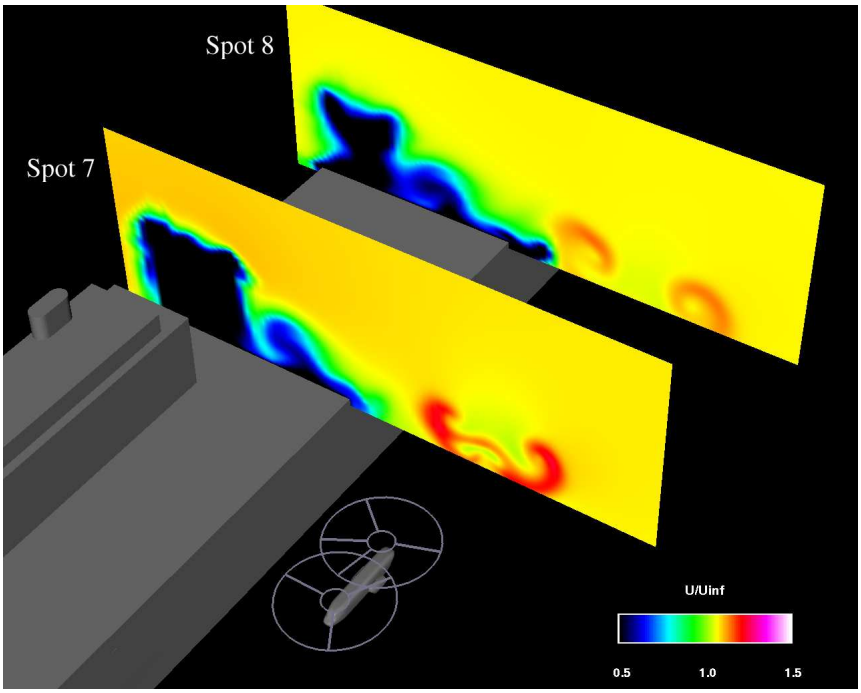

Figure 14: Calculated streamwise velocity component for yaw = 0 deg, Uinf = 19.7 ft/s (35 kts full scale equivalent). CH-46 longitudinal location = Landing Spot 6, lateral offset = 4(b/2), WHOD = 10 ft. Calculations shown for Landing Spots 7 and 8.

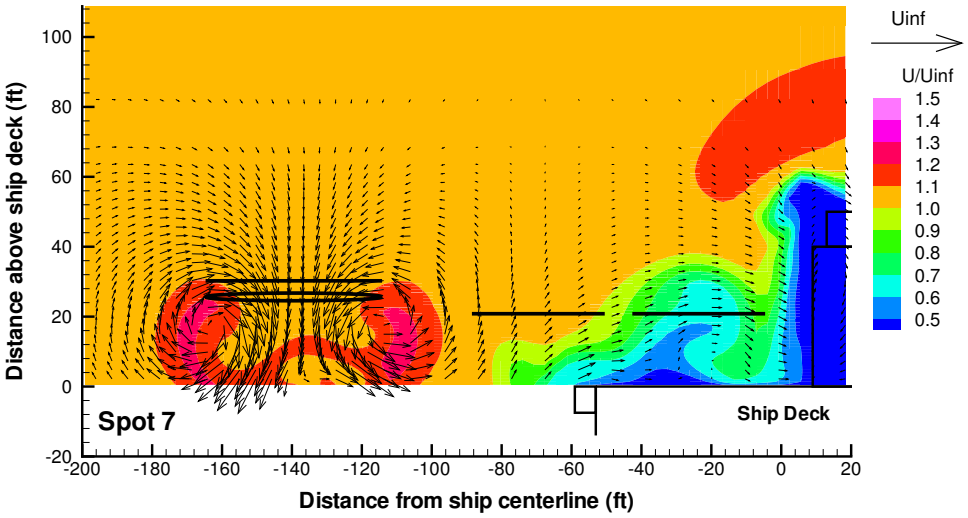

(a) Calculated.

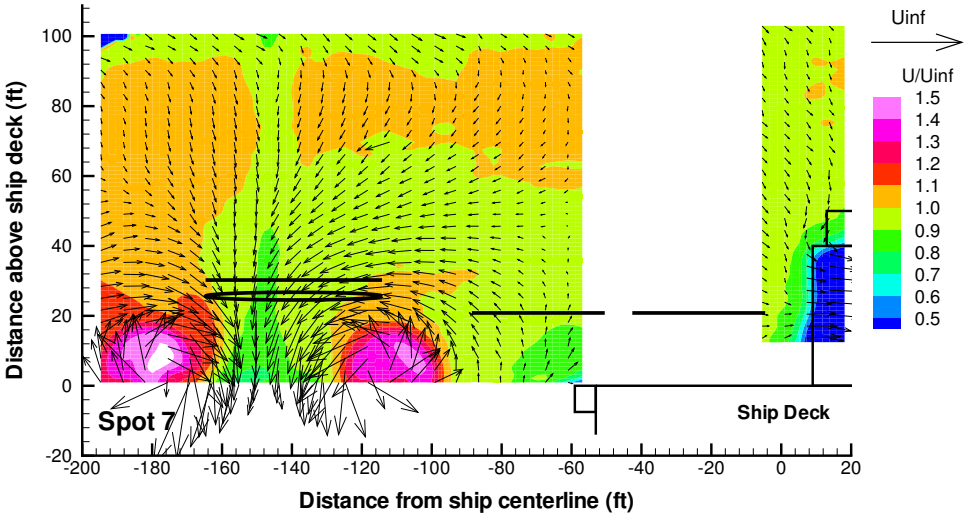

(b) PIV measurements.

Figure 15: Comparison between calculated and measured velocity fields at Landing Spot 7 for yaw = 0 deg, Uinf = 19.7 ft/s (35 kts full scale equivalent). CH-46 longitudinal location = Landing Spot 6, lateral offset = 4(b/2), WHOD = 10 ft. View looking upstream.

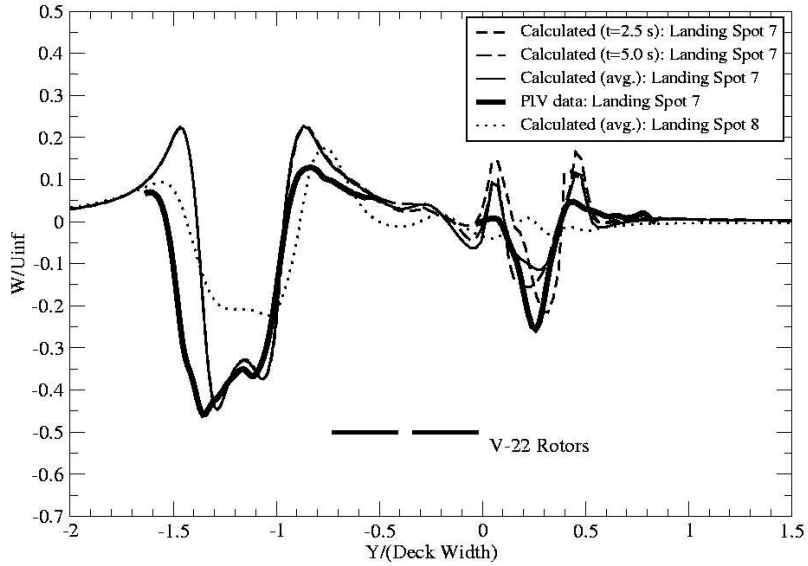

Figure 16: Comparison between calculated and measured vertical velocity for yaw = 0 deg, Uinf = 19.7 ft/s (35 kts full-scale equivalent). CH-46 longitudinal location = Landing Spot 6, lateral offset = 4(b/2), WHOD = 10 ft.

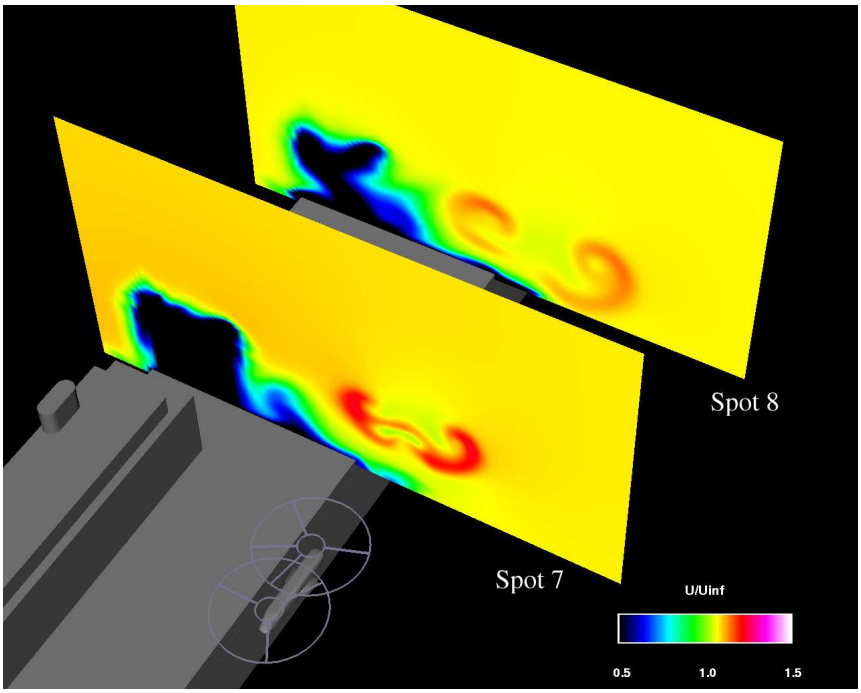

Figure 17: Calculated streamwise velocity component for yaw = 0 deg, Uinf = 19.7 ft/s (35 kts full scale equivalent). CH-46 longitudinal location = Landing Spot 6, lateral offset = 2(b/2), WHOD = 40 ft. Calculations shown for Landing Spots 7 and 8.

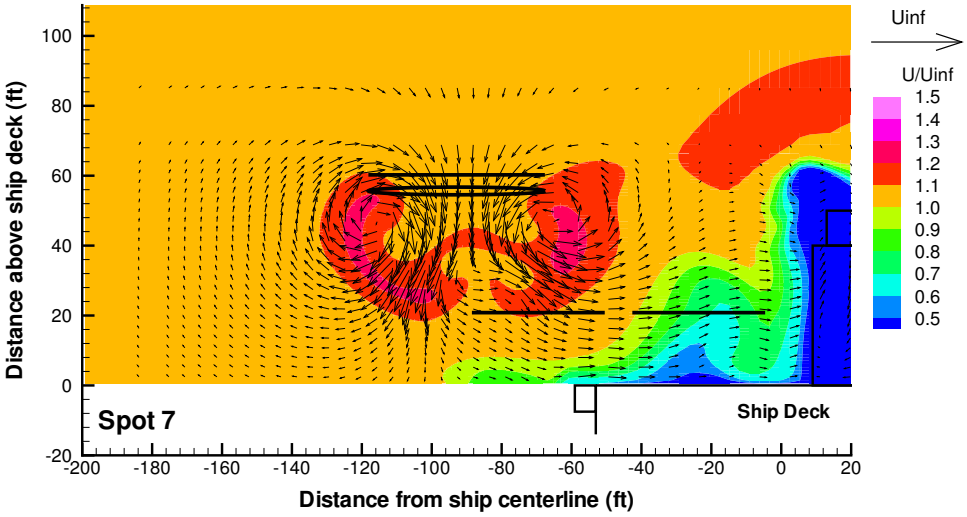

(a) Calculated.

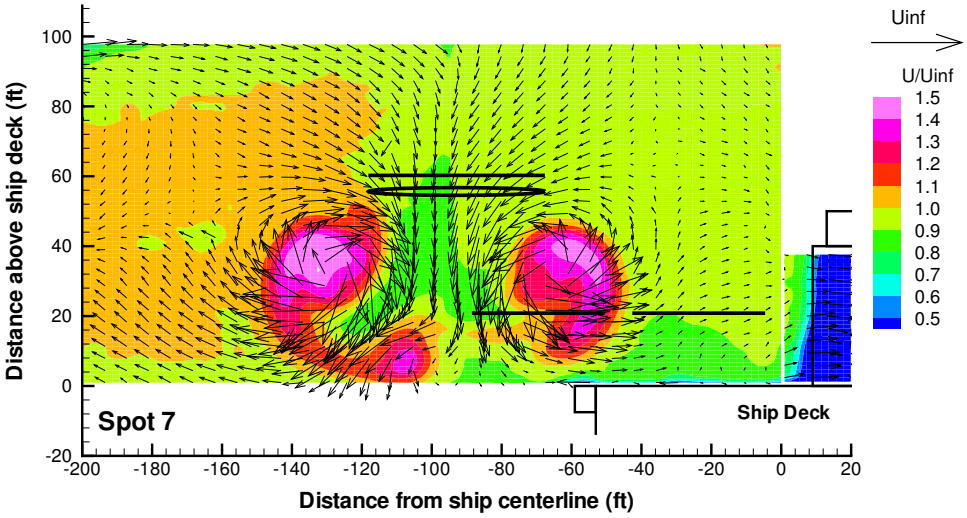

(b) PIV measurements.

Figure 18: Comparison between calculated and measured velocity fields at Landing Spot 7 for yaw = 0 deg, Uinf = 19.7 ft/s (35 kts full scale equivalent). CH-46 longitudinal location = Landing Spot 6, lateral offset = 2(b/2). WHOD = 40 ft. View looking upstream.

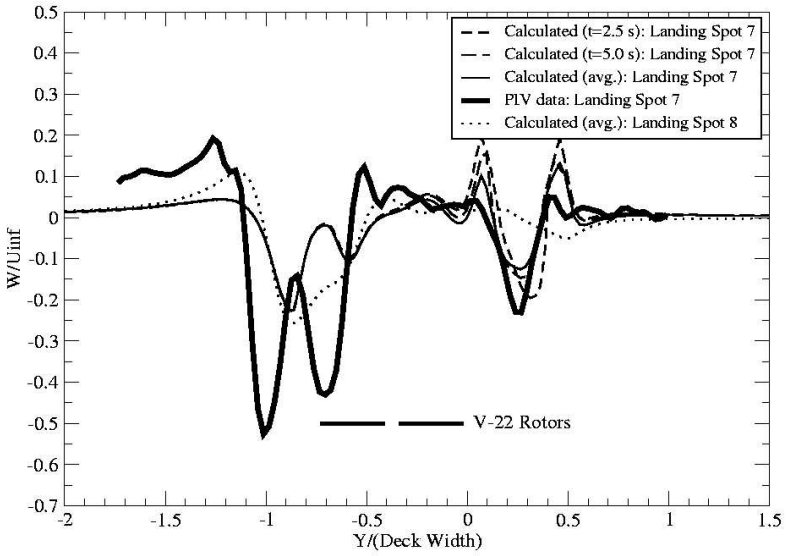

Figure 19: Comparison between calculated and measured vertical velocity for yaw = 0 deg, Uinf = 19.7 ft/s (35 kts full-scale equivalent). CH-46 longitudinal location = Landing Spot 6, lateral offset = 2(b/2), WHOD = 40 ft.

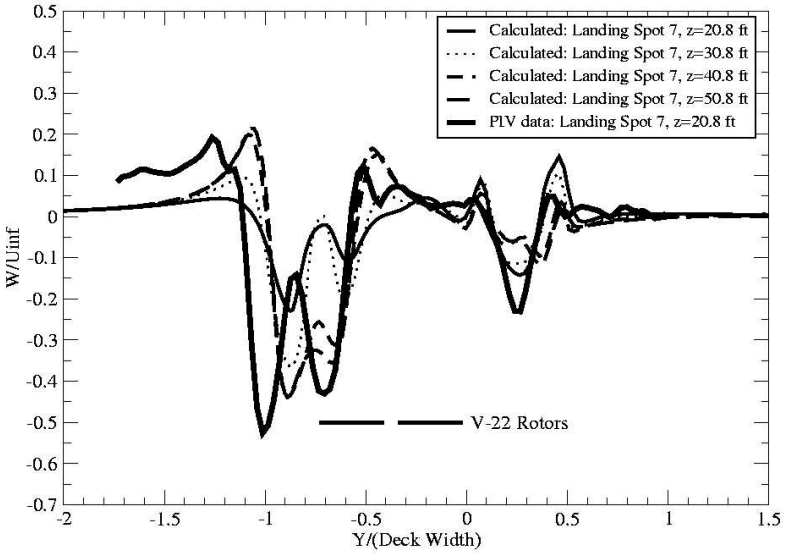

Figure 20: Comparison between calculated and measured vertical velocity for yaw = 0 deg, Uinf = 19.7 ft/s (35 kts full-scale equivalent) at different heights above deck. CH-46 longitudinal location = Landing Spot 6, lateral offset = 2(b/2), WHOD = 40 ft.